Navigation and SAR Auto-focusing Based on the Phase Gradient Approach

Zoran Sjanic, Fredrik Gustafsson
Division of Automatic Control
Department of Electrical Engineering
Linköping University
SE-581 83 Linköping, Sweden
Email: {zoran, fredrik}@isy.liu.se

***Abstract*—Synthetic Aperture Radar (SAR) equipment is an all-weather radar imaging system that can be used to create high resolution images of the scene by utilising the movement of the flying platform. It is therefore essential to accurately estimate the platform's trajectory in order to get good and focused images. Recently, both real time applications and smaller and cheaper platforms have been considered. This, in turn, leads to unfocused images since cheaper platforms, in general, have navigation systems with poorer performance. At the same time the radar data contain information about the platform's motion that can be used to estimate the trajectory and get more focused images. Here, a method of utilising the phase gradient of the SAR data in a sensor fusion framework is presented. The method is illustrated on a simulated example with promising results. At the end a discussion about the obtained results and future work is covered.**

Keywords: Extended Kalman filtering, navigation, Synthetic Aperture Radar, auto-focusing, phase gradient.

I. Introduction

The method of creating high-resolution radar images by utilising the relative motion between imaged scene and a platform that carries the radar, usually an aircraft, is known as Synthetic Aperture Radar (SAR). Typically, during flight, radar echos are collected along the trajectory and saved, giving the Real Aperture Radar (RAR) image with low resolution, see Figure 1. The partial sub images from the RAR image are then integrated to obtain the SAR image with much higher resolution, [1]. This integration can be performed in the frequency domain with Fast Fourier transforms with its advantage of fast processing, [2]–[7]. However, these methods have one major shortcoming, they assume a straight flying trajectory in order to work. In reality, the trajectory will newer be straight, and some other method must be applied, or SAR images will be distorted and back-projection is one of the most known ones, [8]. In the back-projection procedure each saved radar echo, which is one dimensional, is back-projected onto a two dimensional area. In this way a low resolution image of the scene is obtained. Now we can sum up all these back-projected images in order to obtain the full SAR image. Figure 2 describes this procedure in a schematic way. It is now clear that in order to perform the back-projection operation the trajectory of the platform must be known and deviations from the real trajectory will cause the back-projected sub images to be shifted. The summation operation of the sub images will then cause defocusing, which

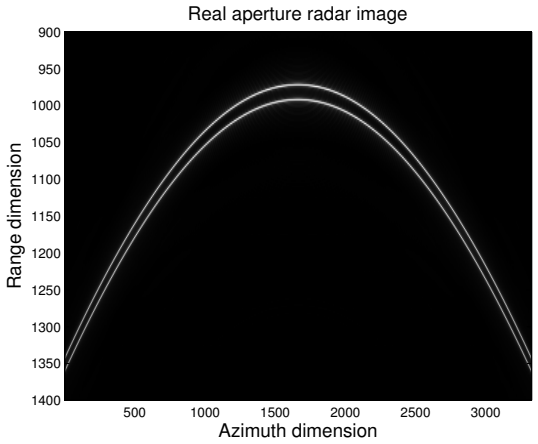

Figure 1: Real aperture radar image (magnitude of the raw radar data) of the two point targets.

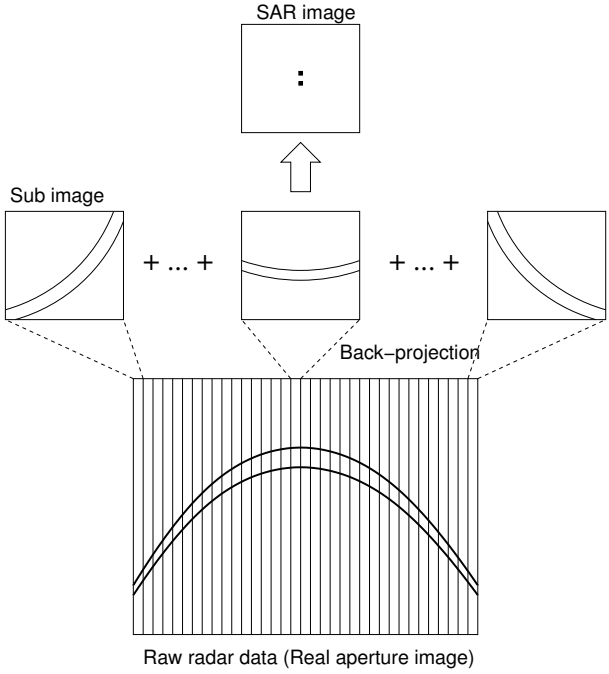

Figure 2: Back-projection operation schematically described.

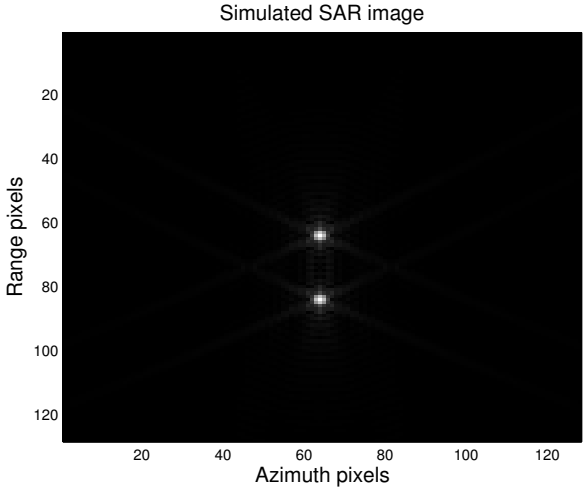

(a) Focused SAR image of two point targets.

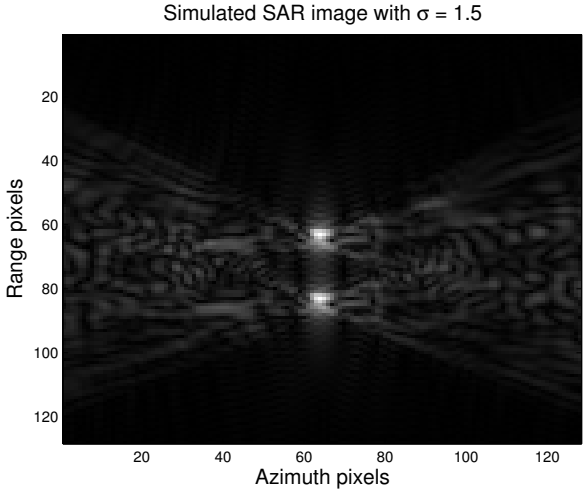

(b) Unfocused SAR image of two point targets with $\sigma = 1.5$.

Figure 3: Example SAR images without and with perturbed trajectory.

is one of the most common SAR image distortions. This is illustrated in Figure 3, where Figure 3a is created using the true trajectory, resulting in a perfectly focused image, while Figure 3b is created using a trajectory where Gaussian white noise $w_t \sim \mathcal{N}(0, \sigma^2)$, $\sigma = 1.5$, is added to the cross-track position of the platform.

The process of correcting for this distortion is called auto-focusing and much effort has been spent on it during recent years, see for example [9]–[13], [15], [16]. Traditionally, these methods are open-loop type, meaning that the image is created with assumptions of linear flight trajectory and focusing is done afterwards in an open-loop way discarding possible flight trajectory information. This is a consequence of the off-line image generating process where the trajectory is no longer interesting. In the setup where SAR images are generated on-line, an idea is to use information from the image defocusing and navigation system together. The approach is to fuse this information in a sensor fusion framework and to try to obtain the best possible solution to both navigation states and image focusing simultaneously.

One approach to simultaneous navigation and auto-focusing is to use complete SAR images to obtain a focus measure as a function of the platform trajectory. This off-line approach is examined in [14] with good results. Since essentially the same information is contained in the raw SAR measurements (RAR images), these can be used for the same goal, *i.e.* auto-focus and extracting the platform's trajectory, but in the on-line setup. Raw SAR data contains phase delay information (which is discarded during image formation), and it is that information that is mainly used for auto-focusing. The methods based on phase information are called Phase Gradient (PG) or Phase Difference (PD) methods. An example of these methods can be found in [16], where phase corrections are done by estimating the phase error by shear averaging of the raw radar data. Slightly different and expanded approach can be found in [10] and [15] where the phase gradient is estimated after the preprocessing of the complete SAR images. Recent work based on phase gradient auto-focus is found in [13] where SAR images are focused with means of the motion compensation obtained from the phase gradient estimate and parametric straight line fitting. One drawback of these approaches is that they are all off-line and basically developed for high frequency SAR systems, where some approximations simplify the focusing process, see Section III for further discussion.

In this work, an on-line trajectory estimation and auto-focusing method for a low frequency SAR system, CARABAS [17], is proposed. The main approach is to fuse the phase information from RAR images and inertial measurement system in the sensor fusion framework and obtain good estimate of the platform's trajectory and in turn focused SAR images. The information from the RAR images is essentially the phase gradient while the inertial information is the acceleration measurements. Note that high precision navigation aid, like GPS, is not used in this setup. However, the proposed method makes it possible to include such measurements as well.

II. Sensor Fusion Framework

A standard approach when using sensor fusion framework is to define a discrete time dynamical model of the system whose states are to be estimated,

$$x_{t+1} = f(x_t, w_t) \tag{1a}$$

$$y_t = h(x_t; \theta) + e_t \tag{1b}$$

where x_t are states of the system, w_t is system noise with variance Q_t, e_t is measurement noise with variance W_t, y_t are measurements, $f(\,\cdot\,)$ describes dynamics of the system and $h(\,\cdot\,)$ is the measurement equation that relates measurements and states of the system. θ is used here to explicitly denote the parametrisation of the measurement equation. In most cases, the dynamics (1a) corresponds to 6-DOF aircraft dynamics. In order to present the main ideas of the proposed approach, the

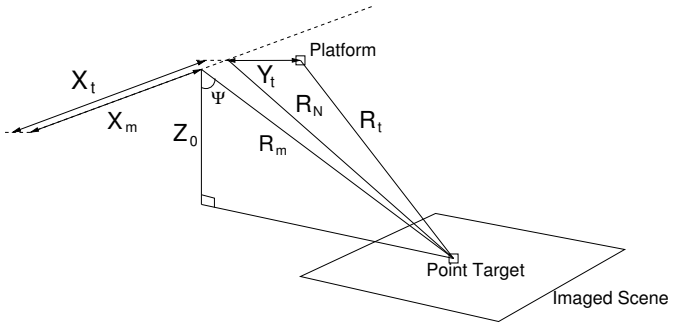

Figure 4: SAR geometry. The figure is not to scale.

much simpler 2-DOF model will be used here, [18],

$$x_{t+1} = Fx_t + Gw_t \tag{2a}$$

$$F = \begin{bmatrix} I_2 & TI_2 & \frac{T^2}{2}I_2 \\ 0_{2\times2} & I_2 & TI_2 \\ 0_{2\times2} & 0_{2\times2} & I_2 \end{bmatrix} \tag{2b}$$

$$G = \begin{bmatrix} \frac{T^3}{6}I_2 \\ \frac{T^2}{2}I_2 \\ TI_2 \end{bmatrix} \tag{2c}$$

$$x_t = [X_t\ Y_t\ v_t^X\ v_t^Y\ a_t^X\ a_t^Y]^T \tag{2d}$$

$$w_t = [w_t^X\ w_t^Y]^T \tag{2e}$$

where T is the sampling time, X is the position in azimuth direction and Y is the position in range direction, v^X and v^Y are the velocities in the X- and Y-directions respectively and a^X and a^Y are the accelerations in X- and Y-directions respectively. w^X and w^Y are the unknown forces acting in the azimuth (X) and range direction (Y) respectively. This is just the discretisised double integrator dynamics. However, the proposed methods are easily extended to the full 6-DOF model with expense of increased complexity. Note that there are no states for the rotation of the platform because the position and orientation of the global frame is arbitrary and here it is assumed to be aligned with the flight direction.

In order to apply the framework, an equation of the form (1b) is also needed. To obtain such equation, the ideas from PG method can be used.

III. Phase Gradient Auto-focusing Method

A. Basics of the PG method

The basis for this approach is the fact that the phase delay of the radar echo data is proportional to the range to the imaged scene, which will vary hyperbolically as a function of time, see Figure 4,

$$\varphi_t = -\frac{4\pi}{\lambda}R_t \tag{3}$$

where λ is the wavelength of the radar carrier. It is seen that phase delay and range are proportionally related to each other. That means that phase and range can be used equivalently, it is only the factor $-4\pi/\lambda$ that differs. We can now calculate the time derivative of the phase delay and obtain

$$\dot{\varphi}_t = -\frac{4\pi}{\lambda}\dot{R}_t \tag{4}$$

The range derivative, $\dot{R}_t$, can be calculated by taking the time derivative of the range R_t that can be expressed as a function of the states, x_t, according to the setup in Figure 4. From the figure it can be seen that the range R_t can, with help from cosine theorem, be expressed as

$$R_t = \sqrt{R_N^2 + Y_t^2 - 2R_N \sin(\Psi)\, Y_t} \tag{5a}$$

$$R_N = \sqrt{R_m^2 + (X_m - X_t)^2} \tag{5b}$$

By using the chain rule we obtain

$$\dot{R}_t = \frac{-(X_m - X_t)v_t^X + Y_t v_t^Y - R_N \sin(\Psi) v_t^Y}{R_t} + \\ + \frac{Y_t \sin(\Psi)(X_m - X_t)v_t^X}{R_N R_t} \tag{6}$$

In the SAR applications where radar frequency is high or antenna size is large, the lobe is narrow and an approximate expression for the range and its gradient can be used without much loss of accuracy. The source of the approximation in this case is the fact that the synthetic aperture length, $2X_m$, and deviation Y_t are much shorter than the range to the middle of the scene, R_m. The range can then be approximated with the Taylor expansion as

$$R_t \approx R_m + \frac{(X_m - X_t)^2 + Y_t^2}{2R_m} - \sin(\Psi)Y_t \tag{7}$$

where all the terms with R_m^2 in the denominator are neglected. Now the range gradient can be calculated from this approximate expression. By using $X_t = v_0^X t$ and $Y_t = v_0^Y t + 0.5\, a_0^Y t^2$, *i.e.* the acceleration a_t^X is zero and velocity in X-direction and acceleration in Y-direction are constant (reasonable assumptions for short aperture times) the gradient becomes

$$\dot{R}_t \approx \frac{-(X_m - v_0^X t)v_0^X + (v_0^Y t + 0.5 a_0^Y t^2)(v_0^Y + a_0^Y t)}{R_m} - \\ - \sin(\Psi)(v_0^Y + a_0^Y t) \approx \tag{8a}$$

$$\approx -\frac{X_m v_0^X}{R_m} - \sin(\Psi)v_0^Y + \\ + \left(\frac{(v_0^X)^2 + (v_0^Y)^2}{R_m} - \sin(\Psi)a_0^Y\right)t \tag{8b}$$

where terms in t^2 and t^3 has been neglected in (8b). The PG methods try to estimate the slope and constant term of this affine function in t from the raw data in order to compensate for the phase delay error caused by the platform's unknown motion, as in *e.g.* [9] or [13]. This compensation is then applied during image formation in order to focus the image. For the time domain image formation approach, this is equivalent to estimating the unknown motion. The assumption made above about narrow radar lobe is not applicable to the SAR systems which operate with low frequency. This will imply that range gradient cannot be approximated with the linear function except in the narrow band around zero phase delay. Due to this, the method of fitting a linear function in order to compensate for the phase delay error described above will not work satisfactory for low frequency SAR. That is why the exact expression for the range is used here.

If we look at the equation (6) we see that the right hand side consists of states of the dynamical model, *i.e.* positions, velocities and some (known) constants. The left hand side of the equation is the entity that can be estimated from the SAR data (either raw or partially processed) which will be explained in the next subsection. This implies that we have a measurement equation from the standard sensor fusion framework in the form (1b) with $\theta = [R_m \ X_m \ \Psi]^T$, and some standard sensor fusion methods, such as the Extended Kalman Filter (EKF), can be applied.

B. Estimating the Phase/Range Gradient

In order to create measurements, y_t, in (1b), we need an estimate of the phase delay gradient. The phase delay gradient estimation kernel, proposed in [16], is (superindex m stands for measured)

$$\dot{\varphi}_t^m = \frac{1}{T} \arg \left\{ \sum_R I_{\text{RAR}}(R,t) I^*_{\text{RAR}}(R, t-T) \right\} \tag{9}$$

where $I_{\text{RAR}}(R,t)$ is the complex RAR image, *i.e.* raw radar data, see Figure 1, I^* denotes the complex conjugate, R is the range dimension, t is the azimuth (or time) dimension and T is the time between radar pulses which is the inverse of the pulse repetition frequency (here used as a sampling time). The motivation for this approach is the fact that the complex raw radar data, $I_{\text{RAR}}(R,t)$, can be written in polar coordinates as

$$I_{\text{RAR}}(R,t) = |I_{\text{RAR}}(R,t)| e^{i\varphi_t} \tag{10}$$

where φ_t is defined in (3), see even [9]. The estimate (9) can be then interpreted as the first order difference approximation of the derivative $\dot{\varphi}_t$. This estimate can be calculated in a sequential manner, pulse by pulse and be interpreted as a measurement y_t for each time instance and used in the sensor fusion framework. This estimation kernel is developed for the high frequency SAR systems where phase gradient can be approximated with a linear function. Since this is not the case in the low frequency SAR system some other method must be applied. If seen in the context of back-projection and sub image processing described in Section I, if each radar echo is used to generate a sub image, the complete SAR image is then simply the sum of all sub images. Each sub image is created with some assumption about range from the platform to the scene, either correct or perturbed, and the raw data contain information about the correct range. This in turn means that each (complex valued) pixel in the back-projected sub image will contain information about the range between the platform and the scene. Nevertheless, due to the phase wrapping effect in the complex number arithmetic, the absolute value of the range cannot be obtained. However, it is possible to estimate the range derivative from the consecutive sub images in a

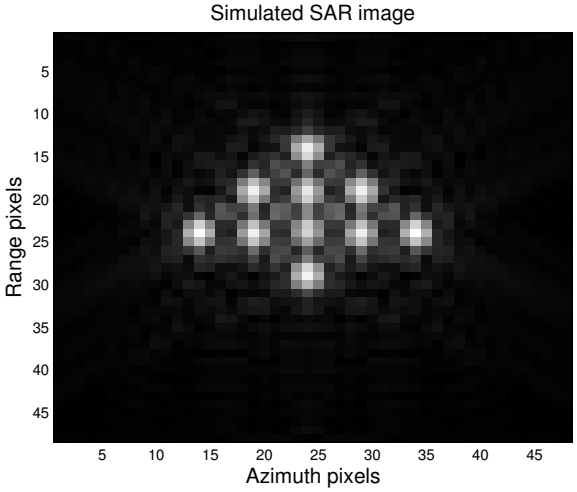

Figure 5: Simulated SAR image of the scene with 10 point targets.

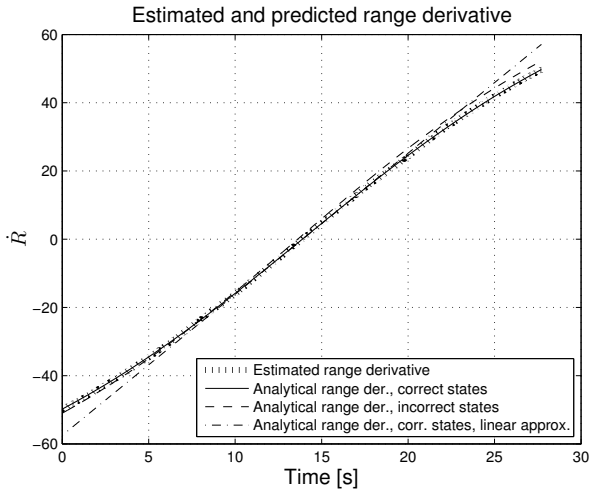

(a) Range derivative, the whole trajectory.

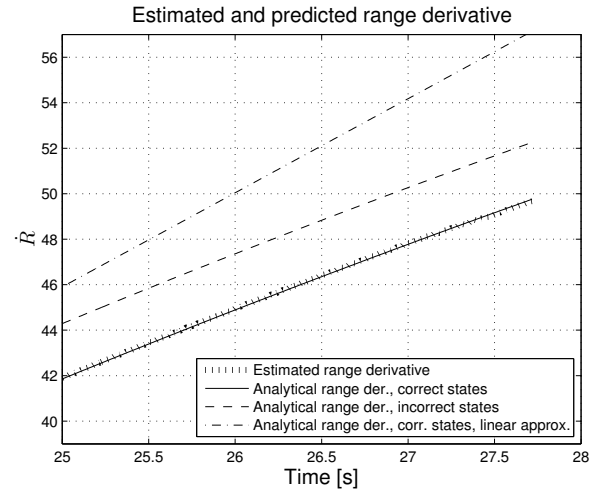

(b) Range derivative, only the last few seconds of the trajectory.

Figure 6: Range derivative estimated from data (dotted line) and calculated with the analytical expression (solid, dashed and dot-dashed lines). Solid line curve is generated with correct trajectory, while dashed is not. Dot-dashed line is generated with approximated expression in (8b).

manner similar to (9) in the following way

$$\dot{\varphi}_t^m = \frac{1}{TM^2}\sum_{i=1}^{M}\sum_{j=1}^{M}\arg\left\{\tilde{I}_{ij}(t)\tilde{I}_{ij}^*(t-T)\right\} \tag{11}$$

where $\tilde{I}_{ij}(t)$ is the complex $M\times M$ sub image generated from radar echo t, see Figure 2, and T is the time between radar pulses as before. This is basically an estimate of the average range to the centre of the imaged scene. The sub image is created with an assumption of straight and constant velocity trajectory with nominal state values. Note that it is only raw data used for the image generation that is summed here, not the whole range dimension as in (9). This is important, if the image to be created is not the same size as the raw data. Range gradient estimated with (11) for the image in Figure 5 is illustrated in Figure 6 (plotted with dotted line) together with analytically calculated range gradients based on (6) (plotted with solid and dashed lines). The one plotted with solid line is based on the correct trajectory, *i.e.* data are collected with the same trajectory used for the analytical expression. For the range gradient plotted with dashed line another trajectory, different from the one used for collecting data, is used. As a comparison, range gradient obtained with the approximated expression (8b) is plotted with dot-dashed line. It is clearly seen that despite correct states are used, the values of this analytical expression deviate from the estimated range gradient in the beginning and the end of the trajectory. This further motivates use of the complete expression for the range gradient, (6). All this gives that the estimate of the range gradient (11) can be interpreted as a measurement y_t and together with (6) as $h(x_t;\theta)$ a standard EKF can be applied.

IV. EKF Auto-focusing and Evaluation of the Performance

A. Extended Kalman Filter

Given the dynamical and the measurement models of the system as in (1), the EKF is defined by the following recursive steps, [19], [20],

$$\hat{x}_{t+1|t} = f(\hat{x}_{t|t},0) \tag{12a}$$
$$P_{t+1|t} = F_tP_{t|t}F_t^T + G_tQ_tG_t^T \tag{12b}$$
$$F_t = \frac{\partial}{\partial x}f(x,w)\Big|_{x=\hat{x}_{t|t},\ w=0} \tag{12c}$$
$$G_t = \frac{\partial}{\partial w}f(x,w)\Big|_{x=\hat{x}_{t|t},\ w=0} \tag{12d}$$
$$\hat{x}_{t|t} = \hat{x}_{t|t-1} + K_t(y_t - h(\hat{x}_{t|t-1})) \tag{12e}$$
$$P_{t|t} = P_{t|t-1} - K_tH_tP_{t|t-1} \tag{12f}$$
$$H_t = \frac{\partial}{\partial x}h(x)\Big|_{x=\hat{x}_{t|t-1}} \tag{12g}$$
$$K_t = P_{t|t-1}H_t^T(H_tP_{t|t-1}H_t^T + R_t)^{-1} \tag{12h}$$

Here $\hat{x}_{t|t}$ is the estimate of the states in the time t given all the measurements up to the time t and $\hat{x}_{t|t-1}$ is the estimate of the states at time t given all the measurements up to the time $t-1$. $P_{t|t}$ and $P_{t|t-1}$ are their respective covariances. Q_t and R_t are considered tuning parameters.

B. Measurement Model

The measurements are the range gradient $\dot{R}_t^m$ obtained from (11) and scaled with factor $-4\pi/\lambda$, and the accelerations in X- and Y-direction. The measurement equation becomes

$$\underbrace{\begin{bmatrix}\tilde{a}_t^X\\ \tilde{a}_t^Y\\ \dot{R}_t^m\end{bmatrix}}_{y_t} = \underbrace{\begin{bmatrix}a_t^X\\ a_t^Y\\ \dot{R}_t\end{bmatrix}}_{h(x_t;\theta)} + \underbrace{\begin{bmatrix}e_t^{a^X}\\ e_t^{a^Y}\\ e_t^{\dot{R}}\end{bmatrix}}_{e_t} \tag{13}$$

where $\tilde{a}_t$ is the measured acceleration, $\dot{R}_t$ is defined in (6) and e_t is white Gaussian noise with covariance matrix $W = \text{diag}\{W_a,\ W_a,\ W_{\dot{R}}\}$. In order to use EKF, the Jacobian of the measurement equation with respect to the states, $\partial h/\partial x$ is needed. For the measurement equation above, the Jacobian is (omitting time index for readability)

$$H = \frac{\partial h}{\partial x} = \begin{bmatrix}\frac{\partial h_1}{\partial X} & \frac{\partial h_1}{\partial Y} & \frac{\partial h_1}{\partial v^X} & \frac{\partial h_1}{\partial v^Y} & \frac{\partial h_1}{\partial a^X} & \frac{\partial h_1}{\partial a^Y}\\ \frac{\partial h_2}{\partial X} & \frac{\partial h_2}{\partial Y} & \frac{\partial h_2}{\partial v^X} & \frac{\partial h_2}{\partial v^Y} & \frac{\partial h_2}{\partial a^X} & \frac{\partial h_2}{\partial a^Y}\\ \frac{\partial h_3}{\partial X} & \frac{\partial h_3}{\partial Y} & \frac{\partial h_3}{\partial v^X} & \frac{\partial h_3}{\partial v^Y} & \frac{\partial h_3}{\partial a^X} & \frac{\partial h_3}{\partial a^Y}\end{bmatrix} \tag{14}$$

and the nonzero elements are (with $\sin(\Psi) = s_\Psi$)

$$\frac{\partial h_1}{\partial a^X} = 1 \tag{15a}$$
$$\frac{\partial h_2}{\partial a^Y} = 1 \tag{15b}$$
$$\frac{\partial h_3}{\partial X} = \frac{v^X + \frac{(X_m-X)v^Ys_\Psi}{R_N} - \frac{Yv^Xs_\Psi}{R_N} + \frac{(X_m-X)^2Yv^Xs_\Psi}{R_N^3}}{R} - \\ - \frac{L(X_m-X)\left(1-\frac{Ys_\Psi}{R_N}\right)}{R^3} \tag{15c}$$
$$\frac{\partial h_3}{\partial Y} = \frac{v^Y + \frac{(X_m-X)v^Xs_\Psi}{R_N}}{R} + \frac{L\left(Y - R_Ns_\Psi\right)}{R^3} \tag{15d}$$
$$\frac{\partial h_3}{\partial v^X} = -\frac{X_m - X - \frac{(X_m-X)Ys_\Psi}{R_N}}{R} \tag{15e}$$
$$\frac{\partial h_3}{\partial v^Y} = \frac{Y - R_Ns_\Psi}{R} \tag{15f}$$
$$L = (X_m-X)v^X - Yv^Y + v^YR_Ns_\Psi - \\ - \frac{(X_m-X)v^XYs_\Psi}{R_N} \tag{15g}$$

C. Numerical Results

Using the dynamic model (2) and the measurement model (13), an EKF has been applied to two cases, one where range gradient measurement has not been used and one where it has. In order to simulate somewhat more realistic acceleration measurements, a bias of $5\cdot10^{-3}$ m/s^2 is added to the X-direction and $-5\cdot10^{-3}$ m/s^2 to the Y-direction in addition to the i.i.d. Gaussian noise, $e_t^a \sim \mathcal{N}(0, 3.6\cdot10^{-3})$. The bias and measurement noise values are chosen as representative for the inertial sensors in the interesting performance class. The performance is then assessed in terms of Root Mean Square

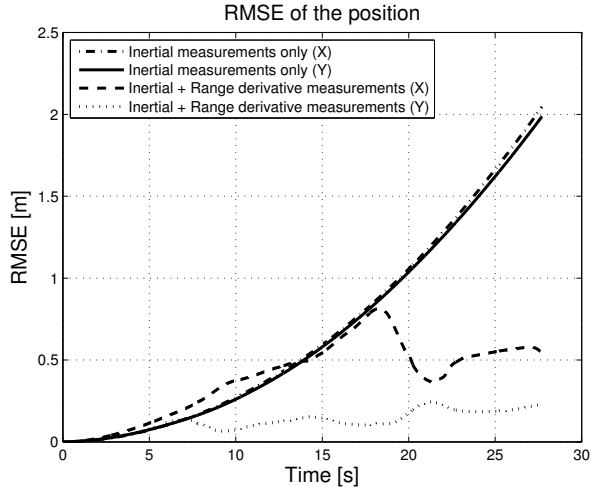

(a) RMSE for the EKF estimated position for the example scene.

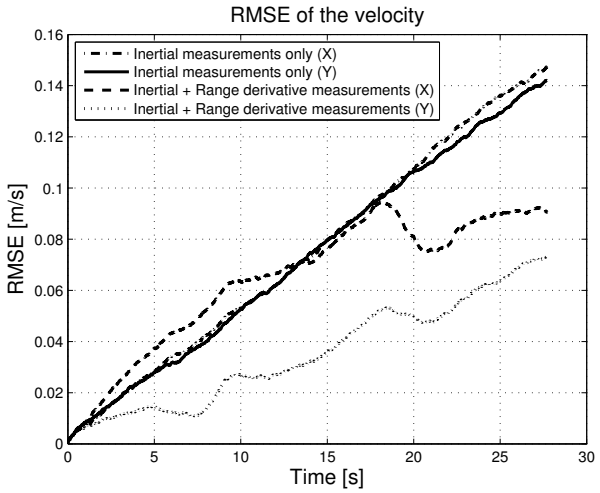

(b) RMSE for the estimated velocity for the example scene.

Figure 7: RMSE for the estimated position and velocity for the example scene. X is the azimuth (or along track) dimension and Y is the range (or cross track) dimension.

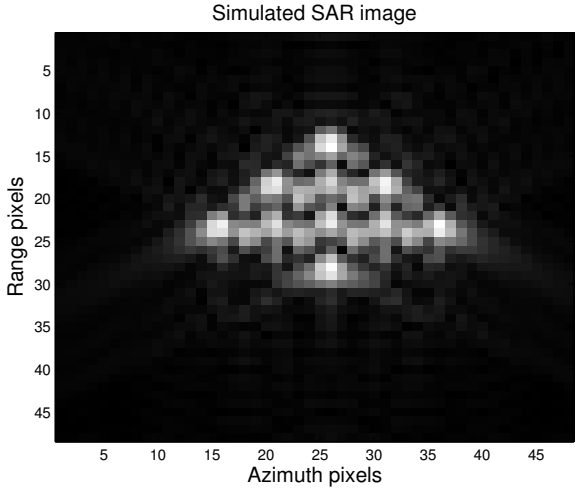

(a) Image of the example scene created with trajectory from the pure inertial estimate.

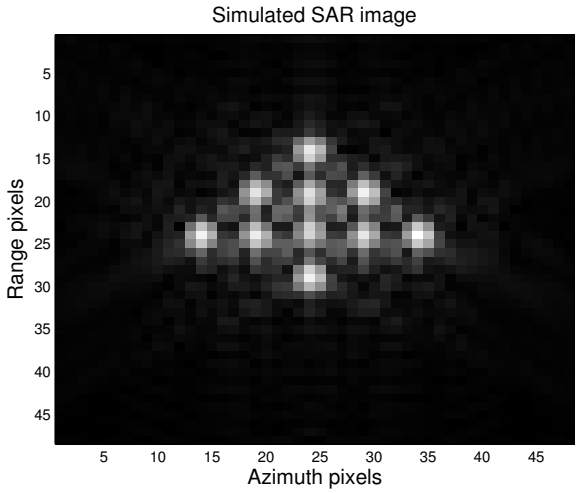

(b) Image of the example scene created with trajectory from the estimate with range gradient as additional measurement.

Figure 8: Images of the example scene created with estimated trajectories with and without range gradient measurement.

Error (RMSE) of the trajectory and mean of the error SAR image power. The RMSE is defined as

$$\text{RMSE}(\hat{x}_t) = \sqrt{\frac{\sum_{k=1}^{N}(\hat{x}_t^k - x_t)^2}{N}} \tag{16}$$

where $\hat{x}_t = [\hat{x}_t^1, \ldots, \hat{x}_t^N]^T$, are unbiased estimates of the scalar parameter x_t (which is a function of time). The error SAR image power is defined as

$$E_{\hat{I}} = \frac{\sum_{i=1}^{M}\sum_{j=1}^{N}|\hat{I}_{ij} - I_{ij}|^2}{MN} \tag{17}$$

where $\hat{I}$ is the $M \times N$ complex SAR image obtained with the estimation procedure and I is the perfect focused SAR image, *i.e.* created with the true trajectory.

The RMSE for the position and velocity based on the 30 Monte Carlo EKF runs as a function of time for cases with and without range gradient measurement is depicted in Figure 7a and Figure 7b. The mean of the SAR error image power obtained from these 30 Monte Carlo runs is 384.1 for the case with range gradient included as a measurement and 2690 for the case with only inertial measurements. The resulting images created with one of the 30 estimated trajectories are depicted in Figure 8. The error image power is 2620 for the image in Figure 8a and 323 for the image in Figure 8b. These images clearly show that addition of the range gradient measurement improves the image focus and the estimate of the navigation states, especially compared to the pure inertial estimates.

As a comparison, an approximate expression of the range derivative (8a) is used as $h(x_t;\theta)$ in a measurement equation and EKF is run. In order to obtain the measurement equation as a function of the states, $X_t = v_0^X t$, $Y_t = v_0^Y t + 0.5 a_0^Y t^2$ and $v_t^Y = v_0^Y + a_0^Y t$ are used giving the nonzero elements of

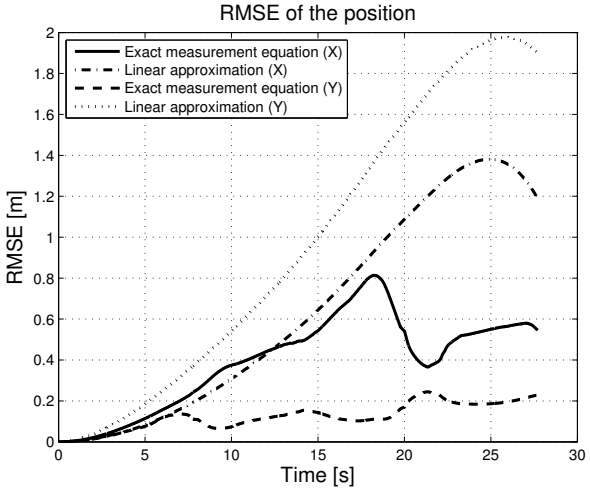

Figure 9: RMSE for the estimated position with approximate and exact range derivative expression. X is the azimuth (or along track) dimension and Y is the range (or cross track) dimension.

the Jacobian (14) as

$$\frac{\partial h_1}{\partial a_t^X} = 1 \tag{18a}$$

$$\frac{\partial h_2}{\partial a_t^Y} = 1 \tag{18b}$$

$$\frac{\partial h_3}{\partial X_t} = \frac{v_0^X}{R_m} \tag{18c}$$

$$\frac{\partial h_3}{\partial Y_t} = \frac{v_t^Y}{R_m} \tag{18d}$$

$$\frac{\partial h_3}{\partial v_t^Y} = \frac{Y_t}{R_m} - \sin(\Psi) \tag{18e}$$

The results from this simulation are presented in Figure 9. It can be seen that estimate with exact expression has much better RMSE value than the one with approximate expression which is even worse than pure inertial estimate. Here, the tuning of the measurement noise, R_t, was changed to eight times higher value in order to get somewhat comparable values (same tuning produces RMSE values in order of 20 m). These results clearly demonstrate the importance of the exact expression for the range derivative.

V. Conclusions and Future Work

Here, a method of simultaneous navigation and low frequency SAR auto-focusing based on a sensor fusion framework is presented. The basis for the approach is the gradient of the range between flying platform and the scene which is used as a measurement in a nonlinear filtering setup. It has also been shown that it is important to use the exact expression for the range gradient instead of the linear approximation common in the high frequency SAR where the lobe is narrow. The average performance in terms of the trajectory RMSE and the focused images is significantly improved compared to the ones based on pure dead-reckoning, without high precision navigation aids like GPS. The RMSE of the position has been largely reduced, as well as of the velocity. The image created with the range gradient supported estimate is hardly distinguishable from the correct image, see Figure 8b and Figure 5.

The evaluation of the proposed methods is, at the moment, only done with the simulated SAR and inertial data. In this way, the ground truth is readily available and the evaluation of the performance easily done. However, in order to fully assess the method, the real SAR and inertial data shall be used, and this is the next step in this work.

Acknowledgements

This work has been supported by the Industry Excellence Center LINK-SIC founded by The Swedish Governmental Agency for Innovation Systems (VINNOVA) and Saab AB.

References

[1] L. J. Cutrona, W. E. Vivian, E. N. Leith, and G. O. Hall, "A high-resolution radar combat-surveillance system," *IRE Transactions on Military Electronics*, vol. MIL-5, no. 2, pp. 127–131, April 1961.

[2] J. A. Fawcett, "Inversion of N-Dimensional Spherical Averages," *SIAM Journal on Applied Mathematics*, vol. 45, no. 2, pp. 336–341, 1985. [Online]. Available: http://www.jstor.org/stable/2101820

[3] H. Hellsten and L. E. Andersson, "An inverse method for the processing of synthetic aperture radar data," *Inverse Problems*, vol. 3, no. 1, p. 111, 1987. [Online]. Available: http://stacks.iop.org/0266-5611/3/i=1/a=013

[4] L. E. Andersson, "On the Determination of a Function from Spherical Averages," *SIAM Journal on Mathematical Analysis*, vol. 19, no. 1, pp. 214–232, 1988. [Online]. Available: http://link.aip.org/link/?SJM/19/214/1

[5] F. Rocca, "Synthetic Aperture Radar: a New Application for Wave Equation Techniques," *Stanford Exploration Project SEP-56*, pp. 167–189, 1987. [Online]. Available: http://sepwww.stanford.edu/oldreports/sep56/56_13.pdf

[6] C. Cafforio, C. Prati, and F. Rocca, "SAR data focusing using seismic migration techniques," *IEEE Transactions on Aerospace and Electronic Systems*, vol. 27, no. 2, pp. 194 –207, March 1991.

[7] A. S. Milman, "SAR Imaging by Omega-K Migration," *International Journal of Remote Sensing*, vol. 14, no. 10, pp. 1965–1979, 1993.

[8] F. Natterer, *The Mathematics of Computerised Tomography*. New York: Wiley, 1986.

[9] C. Oliver and S. Quegan, *Understanding Synthetic Aperture Radar Images*, ser. The SciTech Radar and Defense Series. SciTech, 2004.

[10] D. E. Wahl, P. H. Eichel, D. C. Ghiglia, and C. V. J. Jakowatz, "Phase gradient autofocus - a robust tool for high resolution SAR phase correction," *IEEE Transactions on Aerospace and Electronic Systems*, vol. 30, no. 3, pp. 827–835, July 1994.

[11] L. Xi, L. Guosui, and J. Ni, "Autofocusing of ISAR images based on entropy minimization," *IEEE Transactions on Aerospace and Electronic Systems*, vol. 35, no. 4, pp. 1240–1252, October 1999.

[12] R. L. J. Morrison and D. C. J. Munson, "An experimental study of a new entropy-based SAR autofocus technique," in *Proceedings of International Conference on Image Processing, ICIP 2002*, vol. 2, September 2002, pp. II–441–4.

[13] M. Xing, R. Jiang, X.and Wu, F. Zhou, and Z. Bao, "Motion Compensation for UAV SAR Based on Raw Radar Data," *IEEE Transactions on Geoscience and Remote Sensing*, vol. 47, no. 8, pp. 2870–2883, August 2009.

[14] Z. Sjanic and F. Gustafsson, "Simultaneous Navigation and SAR Autofocusing," in *Proceedings of 13th International Conference on Information Fusion*, Edinburgh, UK, July 2010.

[15] A. F. Yegulalp, "Minimum entropy SAR autofocus," in *7th Adaptive Sensor Array Processing Workshop*, March 1999.

[16] J. R. Fienup, "Phase Error Correction by Shear Averaging," in *Signal Recovery and Synthesis*. Optical Society of America, June 1989, pp. 134–137.

[17] H. Hellsten, L. M. Ulander, A. Gustavsson, and B. Larsson, "Development of VHF CARABAS II SAR," in *Proceedings of Radar Sensor Technology*, vol. 2747, no. 1. SPIE, April 1996, pp. 48–60. [Online]. Available: http://link.aip.org/link/?PSI/2747/48/1

[18] J. Farrell and M. Barth, *The global positioning system and inertial navigation*. McGraw-Hill Professional, 1999.
[19] T. Kailath, A. H. Sayed, and B. Hassibi, *Linear Estimation*. Upper Saddle River, New Jersey: Prentice-Hall, 2000.
[20] F. Gustafsson, *Statistical Sensor Fusion*. Lund: Studentliteratur, 2010.